Sensing of Surface Strain with Flexible Fiber Bragg Strain Gages

Jochen Maul and Tobias Kipp

HBM GmbH, Im Tiefen See 45, 64293 Darmstadt, Germany
Emails: jochen.maul@hbm.com, tobias.kipp@hbm.com

(Extended Information on Optical Strain Sensing using Fiber Bragg Gratings; **May 2011**)

Contents

---

1. Introduction

Due to the extremely high purity of nowadays available optical fibers [1], there is increasing interest in fiber-based sensing instrumentations. Minimal signal loss over long distances (<0.2dB/km) in combination with state-of-the-art precision optics make them attractive for sophisticated sensing applications.

Apart from more traditional optical surface strain detection methods, such as Moiré pattern analysis [2] or contact-free laser-speckle interferometry [3], fiber-based strain sensing methods based on fiber Fabry-Perot sensors [4], on biconically narrowed fibers [5] and on Bragg fibers basically resemble their electrical counterparts in their functionality, but are superior with respect to several metrological properties and performances:

First, they are completely immune against electromagnetic interferences and run without electric power at the measurement site, thus being applicable even in high voltage areas and explosive atmospheres. Second, they exhibit high corrosion and humidity resistance and are therefore usable in wet and harsh environments. From the metrological viewpoint, especially Fiber Bragg Sensors (FBS) show good long-term signal stability, have fastest response times and are suitable for high strain detection (≥ 10,000µm/m). The multi-sensing and multiplexing capability of the fiber-optical technology prevents strong cabling efforts at the measurement location: within a single fiber, several optical sensors can be implemented for measurement of strain as well as of other physical quantities like temperature, pressure, force, weight, displacement, acceleration and torque. They further match quite well with composite materials like carbon faser composites, concrete and laminate which are widely used in modern constructions and architectures, e.g. in aerospace, in wind energy harvesting or in large buildings.

This justifies the increased usage of Fiber Bragg Sensors for strain detection despite some apparent disadvantages compared to electrical strain gages, such as usually higher costs,

stronger temperature susceptibility and lower strain sensitivity. A portrayal of this emerging technology is given e.g. in Ref. [6].

In this contribution, a new class of flexible fiber-Bragg strain sensors is presented together with related fiber-Bragg temperature compensation gages and an optical interrogation technique. The properties and merits of this strain sensing instrumentation are documented and its practicability is outlined.

2. Fiber Bragg Gratings and Bragg Fiber

The Fiber Bragg Grating (FBG) was first demonstrated by Hill et al. in 1978 [7] and meanwhile belongs to the most well-known and most widespread photonic structures in use. In its conception, it is both simple and effective which makes it attractive for lots of applications.

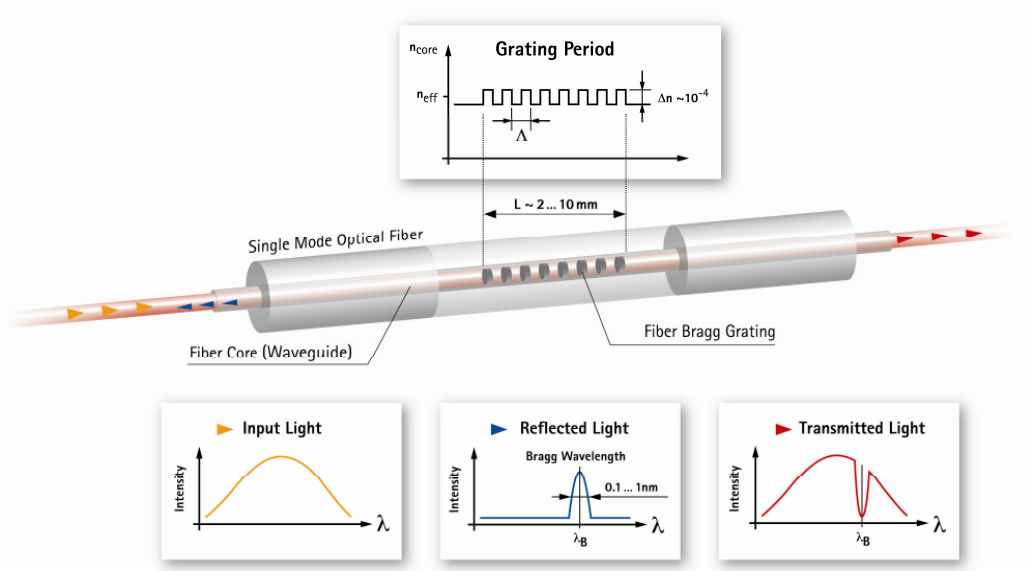

Fig. 1. Principle of a Fiber Bragg Grating (FBG). A Bragg grating is formed by a periodic modulation of the effective refraction index n_{eff} of the optical fiber core. Light around the Bragg wavelength λ_B is reflected back from the grating and therefore misses in the transmission spectrum. Both reflection and transmission signals are amenable to sensing.

The principle of a Fiber Bragg Grating is illustrated in **Fig. 1**. Light conducted by the fiber core is selectively reflected from the Bragg grating and coherently superposed, thus leading to an interference pattern (see also Appendix A3). In general, both the reflection and the transmission spectrum of the Bragg fiber can be exploited for measurements. However, the transmission spectrum suffers from a much larger signal background. Therefore, reflection analysis is standard for the HBM optical equipment.

The basic optical quantities which influence the measured Bragg wavelength λ_B are the grating period Λ and the effective refractive index n_{eff} of the fiber core (see **Fig. 1**), as it is expressed by the fundamental relation of the uniform Fiber Bragg Grating:

$$\lambda_B = 2\, n_{eff}\, \Lambda \qquad (1)$$

The Fiber Bragg Grating originates from a small periodic modulation of the core refractive index n_{core}, such that the effective refractive index n_{eff} is given by the average of an elevated core refractive index n_1 and of the unperturbed core refractive index n_2,

(2) $$n_{eff} = \frac{n_1 + n_2}{2}.$$

There are different accesses to realize a periodic modulation of the core refractive index by pulsed laser irradiation, mainly either by fiber illumination through a periodic phase mask or by a so-called Talbot interferometer where two laser pulses produce a periodic interference pattern at the fiber position [8,9]. The pulsed laser irradiation induces a permanent periodic change in the refractive index of the fiber core either by activating dopants or by introducing morphologic defects into the fiber core at high laser fluences. Depending on the laser fluence used for inscription, weak and strong gratings are distinguished, with Bragg peak reflectivity below ~30% and above ~90%, respectively.
In the case of weak gratings, the dominant Bragg peak at λ_B is typically accompagnied by a number of sidebands. The entire reflection spectrum $R(\lambda)$ including all sidebands is described by:

(3) $$R(\lambda) \propto \left| \sin(x(\lambda))/x(\lambda) \right|$$

with $x(\lambda) = \pi N(\lambda - \lambda_B)/\lambda_B$ [11]. Here, N is the number of grating periods Λ per entire grating length L. **Fig. 2** displays both the measured and the calculated reflection spectrum of a weak Bragg grating; the reflectivity at the Bragg peak is around ~15% (absolute). Sidebands are usually more than one order of magnitude (>3dB) more damped than the main peak which is used as signal.

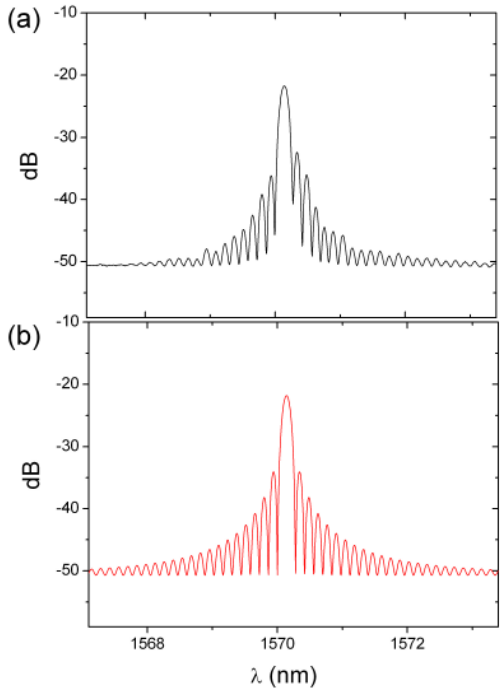

Fig. 2. (a) Measured reflection spectrum of a Fiber Bragg Grating.
(b) Calculated reflection spectrum with Bragg peak and symmetric sidebands around the Bragg wavelength λ_B~1570nm.

This type of weak Bragg grating fiber is used as the basis of the HBM fiber-optical sensors, with a grating length of L~6mm and n_{eff}~1.46. Germanium is used as a dopant inside the fiber core [10] necessary for inscribing Bragg gratings by two interfering ultraviolet laser pulses. The Bragg wavelengths λ_B are chosen in the range of telecommunication wavelengths between 1500nm and 1600nm where optical losses are at a minimum. Correspondingly, the inscribed grating period Λ, which is the spatial distance between two neighboring index modulations, ranges between Λ~510nm and Λ~550nm. At a given grating length of ~6mm, a Bragg grating therefore consists of more than 10000 grating periods.

The core diameter of the Bragg fiber is 5µm, in contrast to 9µm core diameter of conventional telecommunication fibers. This has the advantage that stronger bending is possible due to better compliance with total reflection angles (see Appendix A1). In addition, the Bragg gratings are directly inscribed during the fiber drawing process, followed by a fiber coating process. This Bragg fiber is therefore highly robust and capable of measuring strains above 1%.

3. Bragg Fiber Interrogation and Multiplexing

For telecommunication wavelengths around 1550nm, tuneable laser sources represent a good basis for the interrogation of Fiber Bragg Gratings and Fiber Bragg Sensors. In the HBM interrogators ("optical recorders"), a semiconductor optical amplifier (SOA) is combined with a high-performance fiber Fabry Perot tuneable filter (FFP-TF, a technology from Micron Optics Inc.) to perform a unidirectional ring laser with a maximum tuning range between ~1450nm and ~1650nm. This combination unifies the advantages of high optical gain and broad bandwidth of the SOA with the wide tuning range and the high spectral selectivity of the FFP-TF (free spectral range >200nm).

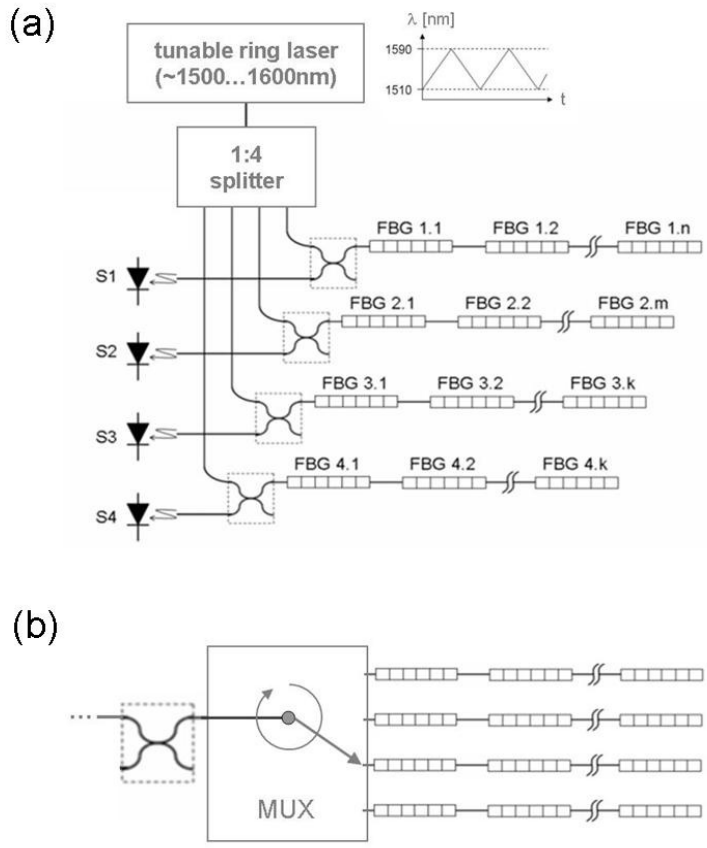

Fig. 3. (a) Scheme of an optical interrogator (4-channel model). Light from a tunable light source is split over 4 channels which couple light to up to 4 fibers with several Fiber Bragg Grating sensors (FBGs 1.1-4.k). The reflection spectrum of the FBGs is recorded by photodiodes (S1-S4). Dotted squares: Fiber couplers for back-reflected light from FBGs. **(b)** Symbolic scheme of an optical multiplexer ("MUX") channel with 1x4 multiplexing capability, connected with one interrogator output channel.

The principal setup of the interrogator is illustrated in **Fig. 3a**. The output of the tuned light source is split over (optionally up to) four optical fiber channels which are connected by one Bragg sensor fiber each. In every chain, light reflected from the Bragg sensors is recorded by

a photodiode which is connected via a fiber coupler. Here, the optical signal is converted into an electrical signal for further data processing. For dynamic interrogation, the FFP-TF is driven with scanning frequencies of up to 1 kHz (e.g. HBM dynamic interrogator DI 410). Static interrogators can achieve 1pm (~1ppm) absolute accuracy by implementation of a NIST certified acetylene gas reference cell (e.g. HBM static interrogator SI 401). All optical interrogators are equipped with either one (series DI/SI 1XX) or four (series DI/SI 4XX) fiber channels.

The number of sensors per chain is typically limited by both the total interrogating range (1510 nm – 1590 nm) and by a reasonable minimum spectral distance of $\Delta\lambda_B$~5nm necessary to prevent mutual signal interference of two neighboring sensor wavelengths after strain and temperature shifts. Hence, a chain with up to 15 Bragg sensors can be connected to each interrogator channel in principle. The standard HBM program is by convention limited to 13 Bragg gratings per chain. For a 4-channel interrogator, the maximum number of sensors therefore amounts to 4x13=52.

The total number of measuring channels can be increased by means of optical multiplexers, as it is sketched in **Fig. 3b**. The 4x8 and 4x16 multiplexers (HBM M408 and M416) for 4 optical input channels and 8 resp. 16 output channels each use a network of 1x2 solid state all-crystal switches which allow fast non-mechanical electro-optical switching with a response time below 0.05 ms. Hence, the maximum number of Bragg sensors of the entire instrumentation is increased to 52x2=104, resp. to 52x4=208.

For dynamic interrogation, the usage of multiplexers however decreases the interrogation rate by a factor equalling the degree of multiplexing, i.e. from 1 kHz to 500Hz for 4x8 multiplexers and from 1 kHz to 250 Hz for 4x16 multiplexers. Furthermore, signal loss reduces the dynamic range to ~40dB for 4x8 multiplexing, resp. to ~30dB for 4x16 multiplexing.

4. Fiber Bragg Sensors – Theoretical Background

Fiber Bragg Gratings are inherently appropriate for sensing strain because the grating period Λ itself serves as a flexible length scale. Any elongation or compression of the Bragg grating translates directly into the strain signal ε when the measured Bragg wavelength shift $\Delta\lambda_B$ is related to the reference Bragg wavelength λ_B:

$$\Delta\lambda_B/\lambda_B = k\cdot\varepsilon \tag{4}$$

The strain $\varepsilon = \Delta L/L$ is thereby given by the relative change in the grating length *L*. Here, the reference Bragg wavelength λ_B is referred to the initial measurement situation, i.e. with typically zero strain and an initial temperature T_0 which remains constant during the strain measurement in the simplest case. The strain sensitivity *k* translates the relative wavelength shift into strain.

In general, both the refractive index n_{eff} and the grating period Λ, and hence also the Bragg wavelength λ_B are affected by strain *and* temperature:

$$\lambda_B(\varepsilon,T) = 2\, n_{eff}(\varepsilon,T)\,\Lambda(\varepsilon,T) \tag{5}$$

Therefore, the absolute Bragg wavelength shift upon thermal and mechanical excitation reads:

$$\Delta\lambda_B(\varepsilon,T) = 2\Lambda n_{eff}\left(\frac{1}{n_{eff}}\frac{\partial n_{eff}(\varepsilon,T)}{\partial\varepsilon}\right)\Delta\varepsilon + 2n_{eff}\,\Lambda\left(\frac{1}{\Lambda}\frac{\partial\Lambda(\varepsilon,T)}{\partial\varepsilon}\right)\Delta\varepsilon$$
$$+ 2\Lambda n_{eff}\left(\frac{1}{n_{eff}}\frac{\partial n_{eff}(\varepsilon,T)}{\partial T}\right)\Delta T + 2n_{eff}\,\Lambda\left(\frac{1}{\Lambda}\frac{\partial\Lambda(\varepsilon,T)}{\partial T}\right)\Delta T \quad (6)$$

Here, $\Delta\varepsilon$ compares initial and final strain. The corresponding relative Bragg wavelength shift yields:

$$\frac{\Delta\lambda_B(\varepsilon,T)}{\lambda_B} = \left(\frac{1}{n_{eff}}\frac{\partial n_{eff}(\varepsilon,T)}{\partial\varepsilon}\right)\Delta\varepsilon + \left(\frac{1}{\Lambda}\frac{\partial\Lambda(\varepsilon,T)}{\partial\varepsilon}\right)\Delta\varepsilon$$
$$+ \left(\frac{1}{n_{eff}}\frac{\partial n_{eff}(\varepsilon,T)}{\partial T}\right)\Delta T + \left(\frac{1}{\Lambda}\frac{\partial\Lambda(\varepsilon,T)}{\partial T}\right)\Delta T \quad (7)$$

This is the complete expression for first-order strain and temperature influences on the relative Bragg wavelength shift. It comprises a set of four optical coefficients (8-11):

$$\alpha_{n\varepsilon} = \left(\frac{1}{n_{eff}}\frac{\partial n_{eff}(\varepsilon,T)}{\partial\varepsilon}\right) \quad (8)$$

$$\alpha_{\Lambda\varepsilon} = \left(\frac{1}{\Lambda}\frac{\partial\Lambda(\varepsilon,T)}{\partial\varepsilon}\right) \quad (9)$$

$$\alpha_{nT} = \left(\frac{1}{n_{eff}}\frac{\partial n_{eff}(\varepsilon,T)}{\partial T}\right) \quad (10)$$

$$\alpha_{\Lambda T} = \left(\frac{1}{\Lambda}\frac{\partial\Lambda(\varepsilon,T)}{\partial T}\right) \quad (11)$$

The photoelastic coefficient $\alpha_{n\varepsilon}$ expresses the change of the refractive index upon strain, the coefficient $\alpha_{\Lambda\varepsilon}$ describes the relative change of the Bragg grating length with elastic strain, the thermo-optical coefficient α_{nT} expresses the thermal change of the refractive index of the fiber core [12], and the (longitudinal) thermal expansion coefficient $\alpha_{\Lambda T}$ expresses the relative length change of the fiber core with temperature.
It is emphasized that these coefficients $\alpha_{...}$ may have physical units different from that of the thermal expansion coefficient α of any materials.

Using available experimental data and theoretical values for the coefficients [12] yields:

$$k := \alpha_{\Lambda\varepsilon} + \alpha_{n\varepsilon} = 1 - 0.21 = 0.79 \quad (12)$$

$$\alpha_T := \alpha_{\Lambda T} + \alpha_{nT} \approx 6.4\times10^{-6}/K \quad (13)$$

In comparison to electrical strain gages, where k~2, the strain sensitivity of the optical Bragg fiber k~0.79 is significantly lower.
The quantity α_T ~ $6.4\times10^{-6}/K$ is a relative wavelength change per Kelvin, but it is not a thermal expansion coefficient itself. It can however be formally related to a thermal expansion

coefficient of α_T/k ~8.1 µm/m/K. The contribution $\alpha_{\Lambda T}$ in α_T is physically related to the thermal expansion coefficient of the pure silica fiber, $\alpha_{silica} = \alpha_{\Lambda T}/k \approx$ 0.55 µm/m/K (resp. $\alpha_{\Lambda T} \approx 0.43\times10^{-6}/K$). Correspondingly, the change of the refractive index with temperature is $\alpha_{nT} = \alpha_T - \alpha_{\Lambda T} \approx 6.0\times10^{-6}/K$ (resp. $\alpha_{nT}/k \approx 7.6$ µm/m/K).

It is interesting to note that the main thermal influence to the wavelength shift originates from the thermal refractive index change and *not* from the thermal fiber expansion (ratio ~1/14).

In total, the temperature-dependent strain signal of the Bragg grating is given by:

$$\frac{\Delta\lambda_B(\varepsilon,T)}{\lambda_B} = k\cdot\Delta\varepsilon + \alpha_T\cdot\Delta T \quad (14)$$

The sketched case only treats the bare silica fiber which is neither bonded to a surface nor embedded in a sensor. However, the entire argumentation also holds for the HBM sensors, as it is expounded in the next chapter.

5. HBM Fiber Bragg Sensors

a. Fiber-optical Strain Gages- Strain Measurement and Stress Analysis

In order to realize a fiber Bragg strain sensor, strain from the substrate needs to be fully transferred to the Fiber Bragg Grating. Therefore, the sensor needs to be tightly bonded onto the surface and the substrate strain has to be completely guided to the fiber. **Fig. 4a** shows the HBM strain sensor which is designed to enable ideal strain transfer into the glass fiber (HBM K-OL). This sensor allows to measure tension and compression without prestrain. The flexible material combination is chosen for sensing of high strain and to enable strain measurements even on bended surfaces, as it is demonstrated in the application example in **Fig. 4b.**

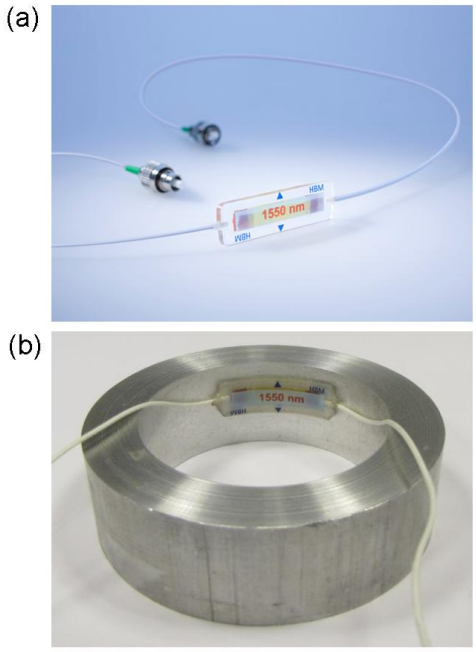

Fig. 4. (a) Optical linear strain gage (HBM K-OL), with two additional fiber connectors. (b) Optical linear strain gage installed onto a ring surface; inner radius = 35mm.

Some basic specifications of this K-OL optical strain gage ("OL") are shown in **Fig. 5**. It exhibits perfect linearity of the Bragg wavelength signal $\Delta\lambda_B/\lambda_B$ upon external strain (**Fig.**

5a). Here, the measured value of the *k* factor is close to the expected value (measured: k=0.78; theoretical: k=0.79; compare eqn. (12)). A continuous-operation test at ±5000µm/m alternating-load on a fiber reinforced plastic (GRP) spring demonstrates the capability of high strain measurement (**Fig. 5b**). The oscillation cycles were repeated 10^7 times, whereupon the full strain was also detected at the end of the cycle. The optical strain gage was also shown to record >±10.000µm/m in single bending tests.

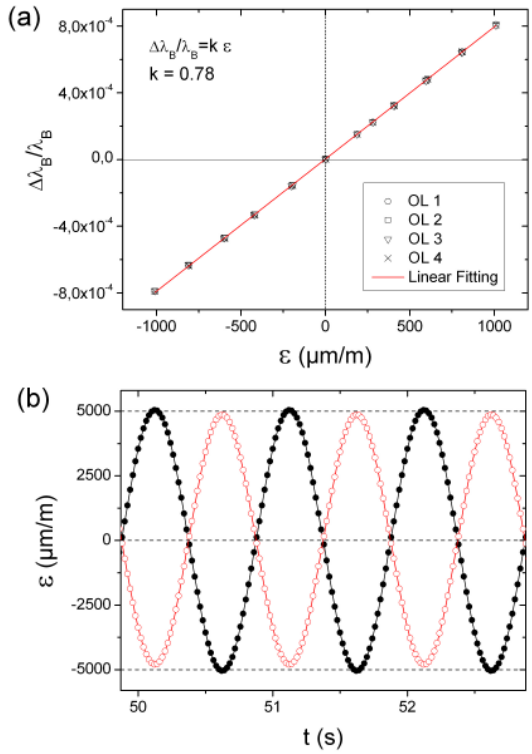

Fig. 5. (a) Linear strain response of optical strain gages ("OL") adhesively bonded on top of a calibrated stainless steel spring. (b) Strain response at ±5000µm/m strain level. Two optical strain gages are therefore bonded on both sides of an oscillating GRP spring.

Since the fiber is guided within the optical strain sensor in a well defined way and tightly bonded onto the specimen surface, the expansion coefficient $\alpha_{\Lambda T}$ of the free Bragg fiber has to be omitted for the bonded sensor. Instead, the thermal expansion coefficient of the specimen α_s has to be taken into account for the total signal of the bonded strain sensor:

$$\frac{\Delta\lambda_B(\varepsilon,T)}{\lambda_B} = k\cdot\Delta\varepsilon + \left(\alpha_{nT}/k + \alpha_s\right)\cdot k\cdot\Delta T\,, \tag{15}$$

where $\Delta\varepsilon$ is the mechanical strain applied to the specimen (compare with eqn. 14). The term α_{nT}/k equals the temperature coefficient of the optical strain sensor (given in the data tables).

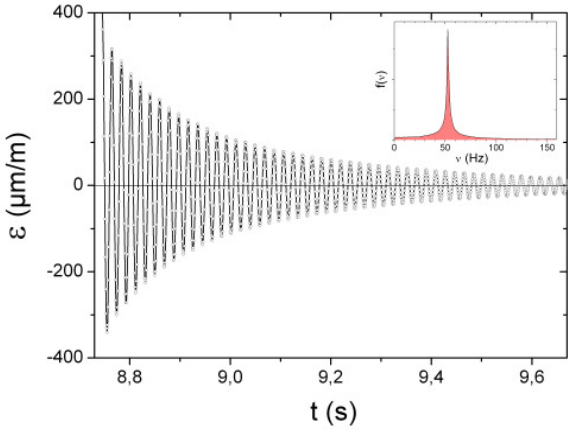

Fig. 6. Dynamic interrogation example of a damped mechanical oscillation recorded by an optical strain gage bonded on top of an aluminium spring. Signal readout is performed by a dynamic interrogator (HBM DI410). The Fourier transform of the oscillation is given as inset.

An example for dynamic interrogation is given in **Fig. 6** where the damped oscillation of an aluminium spring was measured by an optical strain gage using a dynamic 1 kHz-interrogator (HBM DI 410). Here, the Fourier spectrum displays a center frequency around 50Hz and frequency contributions up to ~100Hz.

For two-dimensional strain measurements and subsequent stress analysis, a "rosette-type" optical strain gage ("OR" sensor) is available. Here, three Bragg gratings are inscribed within a sequence. The Bragg fiber is twice bend by 60° and embedded analogue to the linear optical strain sensor, as shown in **Fig. 7** (HBM K-OR).

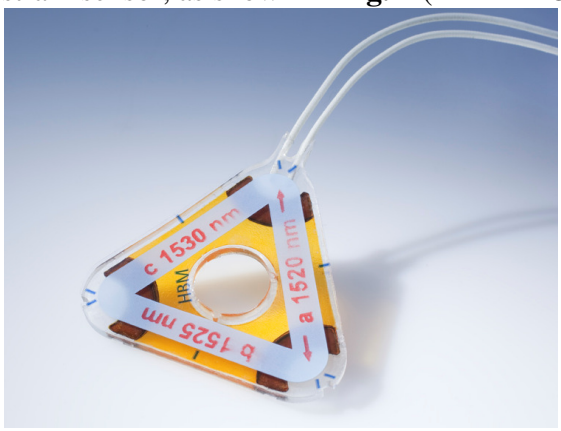

Fig. 7. Optical Rosette sensor with cover and label indicating Bragg wavelengths and clockwise grating arrangements (HBM K-OR).

From the measurement of the strain set $\{\varepsilon_a, \varepsilon_b, \varepsilon_c\}$, the two main normal stress components σ_1 and σ_2 are determined with this 0°/60°/120°- optical rosette sensor by [13]:

$$\sigma_{1/2} = \frac{E}{1-\nu} \cdot \frac{\varepsilon_a + \varepsilon_b + \varepsilon_c}{3} \pm \frac{E}{1+\nu} \cdot \sqrt{\left(\frac{2\varepsilon_a - \varepsilon_b - \varepsilon_c}{3} \right)^2 + \frac{1}{3}(\varepsilon_b - \varepsilon_c)^2} \quad (16)$$

Here, E is the elastic modulus of the measurement body (e.g. E~66kN/mm^2 for Al and E~200kN/mm^2 for most steels) and ν is the inverse Poission ratio between transverse and longitudinal strain upon force in longitudinal direction (e.g., ν~0.33 for Al and ν~0.27 for most steels). The angle φ (**Fig. 8b**) encloses the measuring grating *a* and the stress component σ_1 (see Ref. [13] for details).

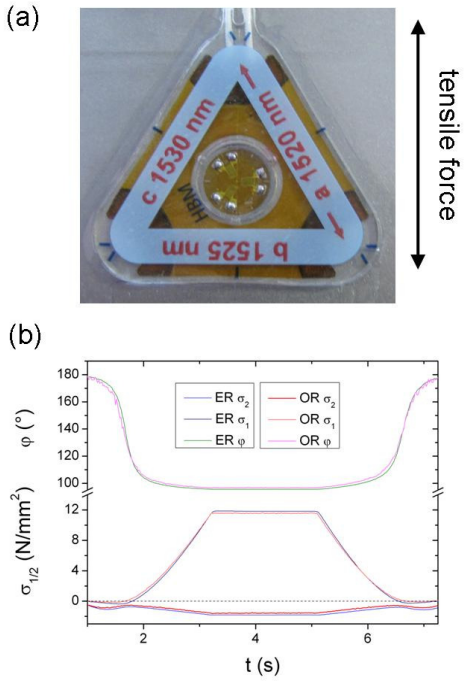

Fig. 8. (a) Measurement configuration to compare optical with electrical rosette strain gage. (b) Comparative stress analysis with optical rosette ("OR") and electrical rosette ("ER"), both mounted on an aluminium tensile bar. The measurement gratings are denoted by "a,b,c". The diagram shows resulting main normal stress components σ_1 and σ_2, and the angle φ between σ_1 and grating *a*.

Fig. 8a shows a measurement configuration used to compare the optical rosette strain sensor with an electrical 0°/60°/120°-rosette strain sensor ("ER" sensor, type HBM RY73-6/120) which are together bonded to an aluminium tensile bar. The two-dimensional strain measurements by both sensors are converted into the stress components σ_1, σ_2 and the angle φ as shown in **Fig. 8b.** Although the optical rosette sensor is larger than the electrical rosette sensor, both stress analyses yield well comparable results.

b. Temperature Compensation Gage

An important prerequisite for precise strain measurements using Fiber Bragg Sensors is an accurate compensation of any thermal influences. This is necessary since the influence of temperature amounts to a Bragg wavelength shift of $\alpha_T \approx 6\,ppm/K$ which compares to a significant temperature-strain signal of 7-8 µm/m/K.
Therefore, a temperature compensation element needs to be placed nearby the strain sensor.
In our approach, temperature compensation can be realized in two ways:

In case of a *known* uniaxial strain direction, a second optical strain gage is used for temperature compensation which is bonded onto the specimen perpendicular to the strain axis (**Fig. 9a**, left). Due to the low transverse strain sensitivity k_t of the optical strain gage compared to the longitudinal strain sensitivity k_l in fiber direction (k_t/k_l <10^{-3}), this gage almost exclusively measures the signal from temperature T and from the transverse contraction of the substrate material which amounts to $\nu \cdot k_l \cdot \varepsilon$. In particular, it exhibits the same temperature characteristics as the optical strain gage bonded in strain direction, i.e. it implies the same temporal temperature response as the optical strain sensor itself.

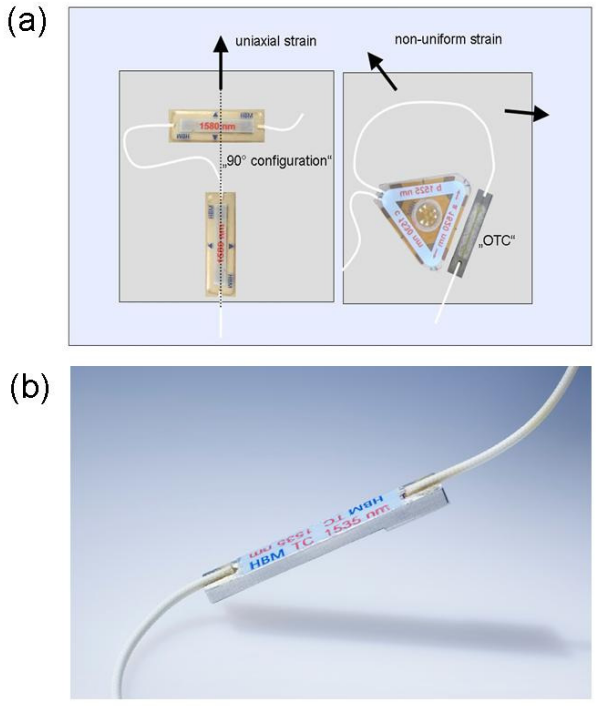

Fig. 9. (a) Temperature compensation with optical strain gage perpendicular to the known uniaxial strain direction (left), and with the OTC sensor in the presence of arbitrary non-uniform strain (right). (b) Optical temperature compensation sensor (HBM K-OTC).

In the presence of an *unknown* strain profile, this procedure is however not applicable. Here, the temperature measurement needs to be completely decoupled from any mechanical specimen strain. In our approach, a special optical temperature compensation ("OTC") gage is therefore designed: The Bragg fiber is mounted on top of an aluminium body which spatially decouples specimen strain from the Bragg grating. The apparent advantage of this sensor is the applicability for any strain profile, but the temperature signal is slightly retarded because

of the finite heat capacity of the sensor body. For the compensation sensor, a time constant of τ~10s for the temperature response upon sudden temperature change at the specimen has to be considered. For comparable temperature conditions, the OTC sensor normally needs to be installed next to the Bragg grating of the optical strain gage, but its alignment angle relative to it is arbitrary (**Fig. 9a**, right).
Both accesses for temperature compensation are demonstrated in **Fig. 9a**; an enlarged view of the optical temperature compensation ("OTC") gage is shown in **Fig. 9b**.

Two central specifications of the OTC gage are obtained from **Fig. 10**. **Fig. 10a** shows a repeated temperature cycle in the operation range between -10°C and 80°C, which is measured as thermal strain by an optical strain gage. The corresponding OTC signal is used for temperature compensation. The temperature compensated strain signal ε' of the optical strain gage (K-OL resp. K-OR) is therefore given by:

$$\varepsilon' = \varepsilon(OL) - \varepsilon(OTC)\cdot \alpha_S / \alpha(OTC) \qquad (17)$$
$$\varepsilon' = \varepsilon(OR) - \varepsilon(OTC)\cdot \alpha_S / \alpha(OTC)$$

Here, $\alpha(OTC) = 30.6\,\mu m/m/K$ is the temperature coefficient of the OTC sensor. α_S [µm/m/K] is the thermal expansion coefficient of the specimen on which the OTC is bonded. In the test measurement of **Fig. 10a**, no mechanical strain is applied such that the pure temperature effect is filtered out. Even at the edge values of the temperature range, the compensation error is below 1%.

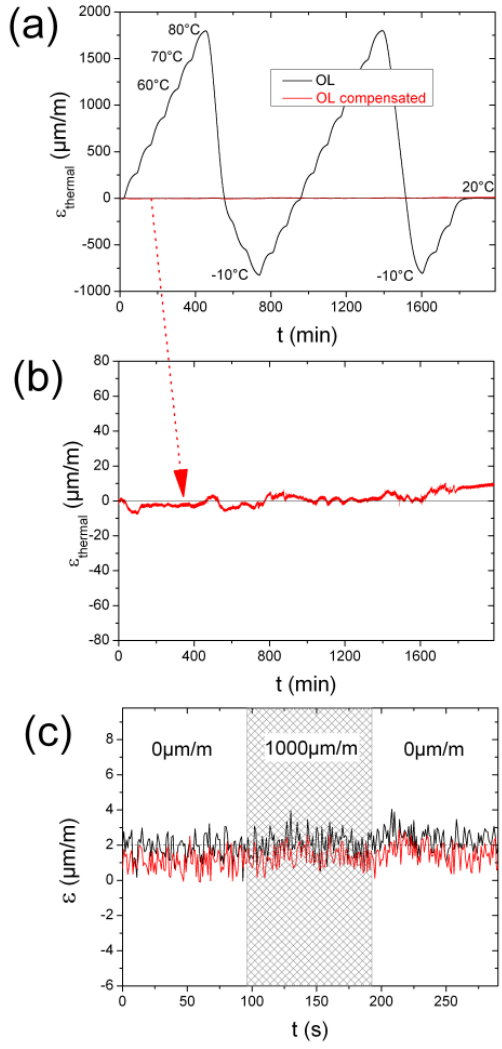

Fig. 10. (a) Temperature-strain signal of an optical linear strain gage (OL), bonded on an aluminium body and exposed to several temperature cycles, and corresponding strain signal after temperature compensation with an OTC gage. (b) Enlarged view: Temperature compensated OL signal. (c) Response of two OTC sensors upon a mechanical strain cycle applied to the specimen.

The absolute temperature compensation error in the complete temperature cycle is below 10µm/m (**Fig. 10b**). In addition, the OTC sensor design effectively decouples mechanical strain from the substrate as shown in **Fig. 10c**. Stretching of the substrate by 1000µm/m evidently effects no change of the OTC signal.

.

Fig. 11 illustrates a combined temperature and strain test where one optical strain gage is bonded on a steel body (α_s=10.8µm/m/K) and temperature compensation is realized with an OTC sensor. Temperature varies irregularly between ~20°C and ~80°C, and two individual mechanical strain events are carried out. The temperature compensated signal basically shows the two mechanical strain signals and a low background from temperature influences (<40µm/m). In this practical test, the time constants for temperature changes occasionally went significantly below τ=10s and therefore lead to a partly enhanced compensation error.

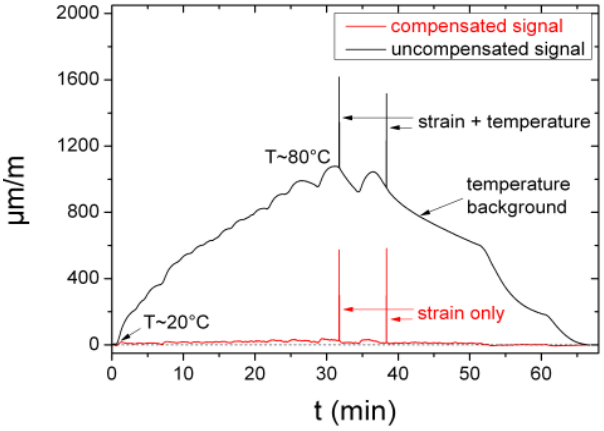

Fig. 11. Temperature compensation test in the presence of mechanical strain. The OL strain sensor was bonded on a steel body and temperature compensation was performed with an OTC gage.

6. Measurement Chain

Fig. 12. shows the Bragg spectrum of a measurement chain example containing a maximum number of 13 Bragg sensors, each adjacent sensor pair separated by a spectral distance of ~ ±5nm. With this spectral distance, strain up to $\pm\Delta\lambda_B/\lambda_B/k$ ~±5nm/1550nm/0.78~±4000µm/m can be measured provided that the neighboring sensors are unstrained. For measurement of higher strain, the Bragg wavelength differences have to chosen to ±10nm or ±15nm.

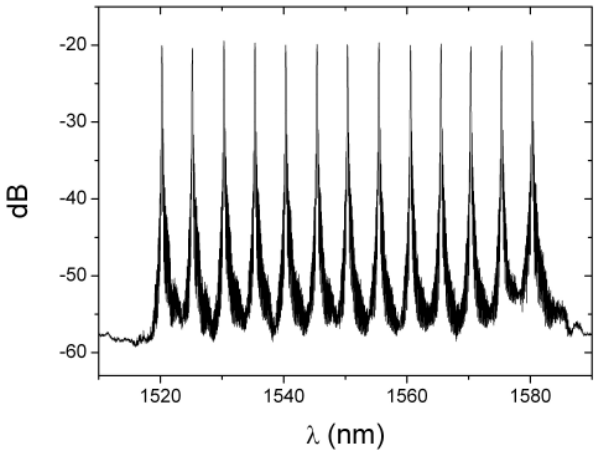

Fig. 12. Optical measurement chain with 13 Bragg gratings separated by a Bragg wavelength difference of $\Delta\lambda_B \approx$ 5nm each. The spatial distance between each pair of Bragg gratings is ~50cm.

Measurement chains are connected to the interrogator by means of standard FC/APC-fiber connectors with ends cut in a 8° angle. This prevents backreflection of signal background into the incoming interrogator fiber by exceeding the total reflection angle (see Appendix A1).

In practice, Bragg sensors are often separated by different fiber lengths connecting various installation spots. Thereby, the sensor fiber has to be elongated by insertion of fiber parts

using optical splices. However, optical losses should be kept below 4dB within the sensor chain in order to avoid ambiguity in Bragg peak detection. This occurs especially when certain sidebands, which lie occasionally up to 4dB below the corresponding Bragg peak level, reach similar intensities as other Bragg peaks in the same chain.

Optical losses appear at different levels, as it is summarized in **Fig. 13**: Whereas the specific loss of the connection fiber (telecommunication fiber) used to connect the interrogator with the sensor chain is as low as 0.2dB/km (one way), the specific loss of the sensor fiber is 9dB/km (one way). Therefore, the total length of the sensor fiber should not exceed ~200m. However, the length of the connection fiber is not critical because it introduces an overall signal damping of *all* Bragg sensors.

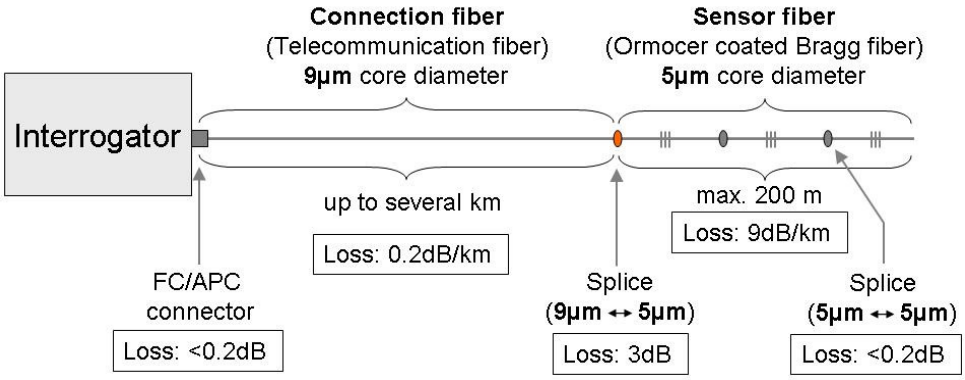

Fig. 13. Recommended fiber length limits and signal losses in a fiber Bragg sensor chain.

Due to optical mode field adaption from the sensor fiber (core diameter ~5µm) to the low-loss telecommunication fiber (core diameter ~9µm), bidirectional optical losses amount to ~3dB for each splice between both fiber types. Therefore, the complete chain should not contain more than one interconnection splice, i.e. fiber types should not be changed more than once per chain. The process of fiber splicing is briefly illustrated in **Fig. 14**. Thereby, both fiber ends are cut in a 0° angle, are then precisely aligned and finally fused by an electrical arc discharge. Splices between the same fiber types only introduce losses typically below ~0.2dB (one way).

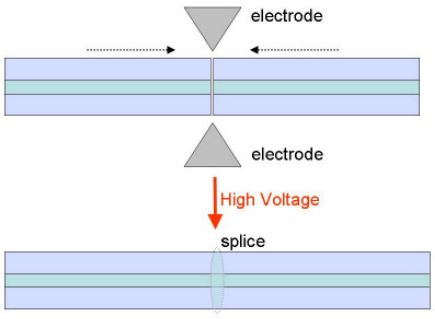

Fig. 14. Process of fiber splicing by an electrical arc discharge optical splicer.

Another source of optical losses is related to critical fiber bending. In this case, the total reflection angle is under-run and light escapes from the fiber core. The critical bending radius is as low as 2 mm for the sensor fiber, but ~20 mm for the telecommunication fiber.

For accurate detection of the Bragg wavelengths, fiber bending and fiber positioning should not be changed too much during the measurement process: The interrogators of the HBM SI/DI series utilize linearly polarized light which may change orientation during fiber bending. Since the Bragg gratings commonly show some rotational anisotropy, changing the

polarization state of light used for interrogation leads to a small polarization shift of the Bragg wavelength up to ~20pm. It is therefore recommended to fix the complete chain at selected locations once all sensors are readily installed.

Finally, a time-of-flight (TOF) correction for the light travelling time can be implemented for long connection fibers in order to obtain absolute strain values: since the DI/SI interrogators rely on a scanning technique, the wavelength scanning time is directly translated into a proportional scanning wavelength at the data acquisition side. Therefore, any additional propagation time of the Bragg signal from the grating to the photodiode due to optical pathways leads to an artificial shift in the detection wavelength. For example, with a speed of light of $c_0/n \sim 2*10^8$ m/s ($c_0=3*10^8$ m/s is the speed of light in air, n~1.5 is the fiber refractive index), light needs ~5ns to pass 1m fiber. The TOF shift becomes especially critical for dynamic interrogation. In case of 1 kHz interrogators, the scanning time for the wavelength range of 80nm amounts to ~0.4ms. For kilometer long connection fibers, the TOF shift can easily reach values in the nm-regime which have to be considered for absolute measurements.

7. Calibration of Optical Interrogators

For calibration of optical interrogators, athermal fiber Fabry Perot etalons are used as an absolute wavelength scale.

The etalon basically consists of two fixed plane-parallel dielectric surfaces which are inserted into the fiber path. They act as a precision wavelength filter through multiple reflections and interference of light rays from the partially reflecting dielectric surfaces. Etalon reflection peaks are described by the Airy function

$$R(\lambda) \propto \left(1 + F \sin^2(\delta/2)\right)^{-1} \tag{18}$$

where the optical phase acquired by the light wave on one round trip through the etalon is given by $\delta = 4\pi n l/\lambda$. Here, n is the index of refraction and l is the distance between both etalon interfaces. The finesse $F = 4R/(1-R)^2$ with the dielectric surface reflectivity R is used to quantify the shape of the etalon reflection peaks. The Free Spectral Range (FSR) $\Delta\lambda$ displays the peak-to-peak distance.

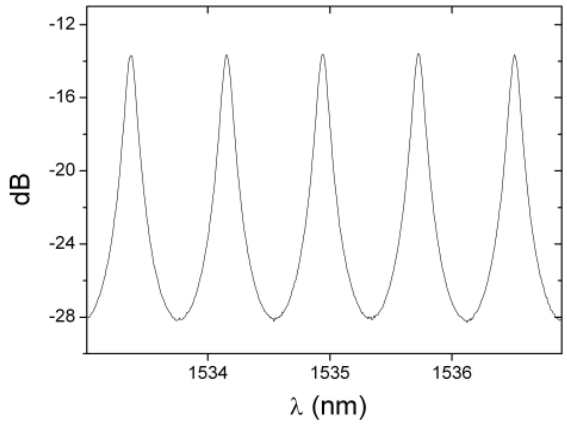

Fig. 15. Section of the fiber etalon reflection spectrum used for interrogator calibration.

Fig. 15 shows a small section of the fiber etalon reflection spectrum recorded by a HBM SI401 interrogator. The etalon peaks are remarkably sharp and therefore precisely define a broad spectrum of calibration wavelengths. They do not change their position with

temperature and they cover the complete interrogation range between 1510 and 1590nm. In the zoomed etalon spectrum of **Fig. 15** the FSR is ~0.8nm around λ_0~1535nm.

By peak wavelengths determination using HBM interrogators which are actively calibrated using an implemented gas cell standard (e.g. the HBM SI401), an absolute calibration of the etalon is performed. This procedure allows to establish a calibration protocol by listing the etalon peak wavelengths measured with a certified gas cell interrogator together with the etalon peaks measured with the interrogator in quest.

For both static and dynamic interrogators, the absolute calibration error is below 10pm (typically ±1-2pm).

8. Anomalies in the Bragg Spectrum

a. Birefringence and Inhomogeneous Strain

In this chapter, some basic effects are described which might lead to failure in Bragg peak recognition or even falsify the Bragg signal.

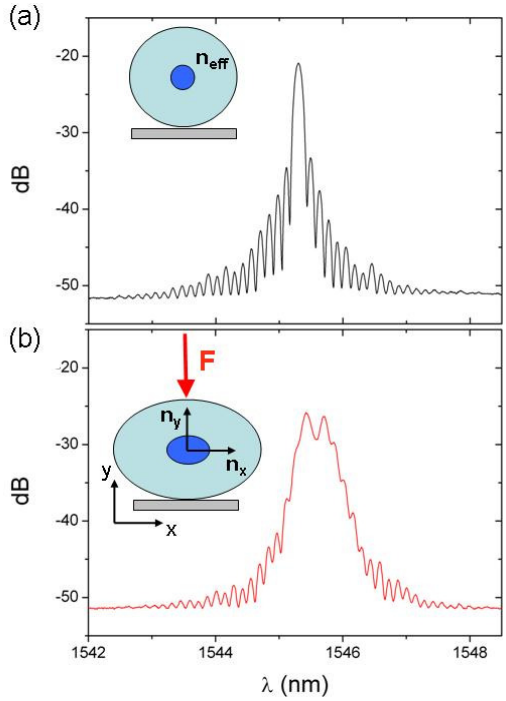

Fig. 16. Bragg spectrum (a) without and (b) in the presence of birefringence. The insets illustrate the change in the core refractive index (a) without and (b) with a transverse force applied to the fiber.

A major source for deficient signal detection is *birefringence* [14]:
Radial forces F per fiber length L (F/L) lead to anisotropic refractive indices n_{eff}^{x} and n_{eff}^{y} in the fiber core (**Fig. 16**). This effects a splitting of the Bragg peak into two separate peaks:

(19) $$\lambda_B^i = 2\, n_{eff}^i (F/L)\, \Lambda \quad (i = x, y)$$

The difference between both refractive indices defines the birefringence β

(20) $$\beta := n_{eff}^{x} - n_{eff}^{y}$$

which directly measures the magnitude of Bragg peak splitting:

(21) $$\Delta\lambda_B(F/L) = 2\Lambda\beta(F/L)$$

For the Bragg fiber used in all above sensors, we find experimentally

(22) $$\beta \approx 3.15 * 10^{-7}\,(F/N)/(L/mm).$$

Fig. 16 shows an unperturbed Bragg peak as well as a double peak due to birefringence. Obviously, birefringence causes an ambiguity in the peak identification process in which the wavelength at peak maximum is depicted. In practice, birefringence may be caused e.g. either by change of the glue properties or by direct application of radial forces.

Strongly inhomogeneous strain profiles may cause a broadening or splitting of the Bragg peak as well: in contrast to electric strain gages, strain affects the Bragg grating *locally* and does not necessarily sum up to a uniform signal peak. This means that a strongly inhomogeneous strain profile, such as e.g. due to microcracks directly underneath the bonded Bragg grating, results in a series of adjacent Bragg peaks.

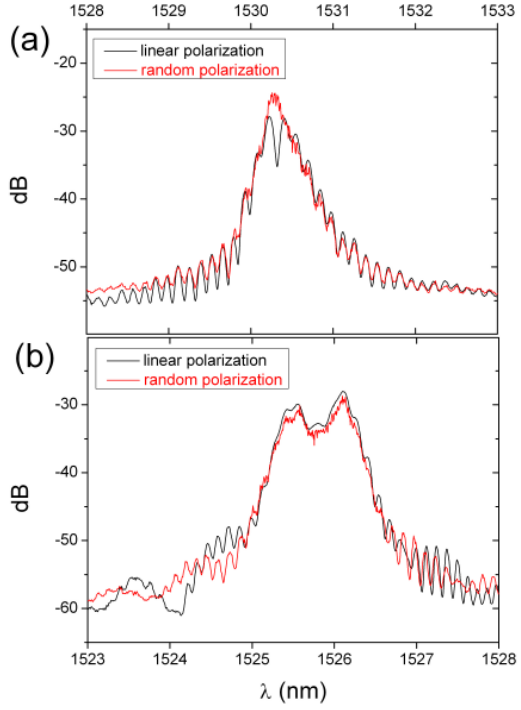

Fig. 17. Bragg signal deformation in the presence of (a) *birefringence* and (b) *inhomogeneous strain profile*.
To distinguish both cases, the Bragg signal was measured with linear and random light polarization. Whereas birefringence only shows peak splitting by using linearly polarized light for interrogation, inhomogeneous strain interrogation is not affected by light polarization.

In this case, the Bragg spectrum is obtained from the Bragg signal average over the spatial strain profile $\varepsilon(z)$ within the grating length L:

(23) $$R(\lambda) \propto \int_L R(\lambda, z)\, dz$$

Here, $R(\lambda, z)$ is derived from eqn. (3) by introducing a spatial strain dependence of the grating period Λ,

(24) $$\Lambda \equiv \Lambda(z) = \Lambda_0\,\varepsilon(z) + \Lambda_0\,.$$

Here, Λ_0 is the period of the unstrained grating. In this sense, the variable $x(\lambda)$ in eqn. (3) becomes $x(\lambda,z)=\pi N\left(\lambda-2n_{eff}\Lambda(z)\right)/\left(2n_{eff}\Lambda(z)\right)$, yielding $R(\lambda,z)\equiv\left|\sin(x(\lambda,z))/x(\lambda,z)\right|$.

To distinguish birefringence from inhomogeneous strain experimentally, an optical scrambler (General Photonics PCD-104) was used to generate random light polarization from the linear light polarization of the interrogator: Since the Bragg wavelength is only sensitive to different anisotropic refractive indices n_{eff}^{x} and n_{eff}^{y} in the presence of *linearly* polarized light, randomization of polarization states leads to the detection of a uniform Bragg peak (**Fig. 17a**). In contrast, Bragg signals from inhomogeneous strain profiles do not depend on the polarization state of light (**Fig. 17b**).

Strongly **inhomogeneous strain** profiles underneath the Bragg grating resp. **lateral fiber forces** can significantly distort the Bragg peak shape and lead to peak detection problems.

b. *Background Modulations from Fiber Ends*

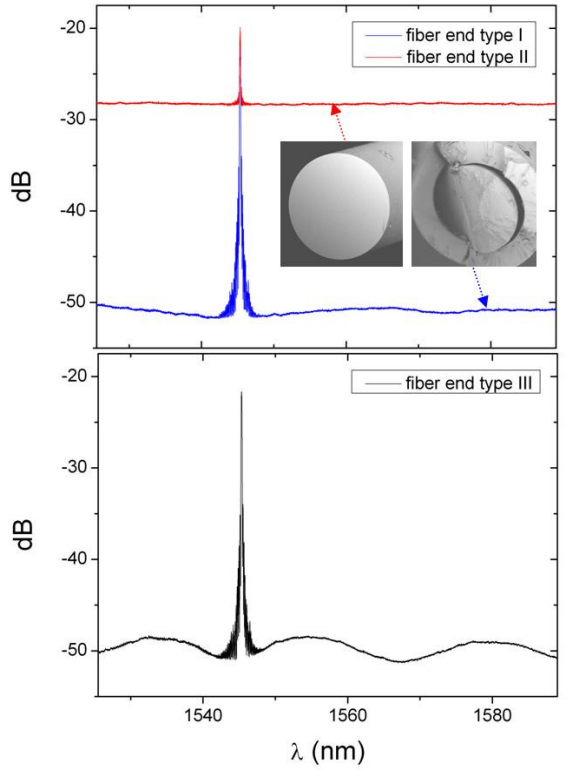

Fig. 18. Backgrounds modulations of the Bragg spectrum. Three types (I-III) are distinguished depending on the morphology of the fiber end. Insets: SEM micrographs of fiber ends attributed to aberrant background modulation of types I and II, as detailed in the text.

Further, the shape of the Bragg fiber *end* influences the signal-to-background ratio because it determines the degree of unselective back-reflection. **Fig. 18.** shows background levels relative to the Bragg peak for different fiber end configurations.

Type I represents an irregular fiber cut with diffuse light reflection at the end for which the lowest background level is obtained. In contrast, type II represents a 0° cut end. Here, ~4% of laser light is reflected back into the fiber at any wavelength and superimposes the Bragg spectrum. In the case of type III, the formation of at least one mirror facet in a small angle to the fiber core likely leads to an interferometric arrangement of the ends of both measurement fiber and coupler fiber (see **Fig. 18**, dotted frames). The period of the resulting background oscillation appears therefore characteristic for the fiber cutting angles.

Since **background modulations** stem from regular **fiber end cuts**, they can be avoided in practise by irregular cuts and subsequent sealing of the fiber ends.

9. Applications

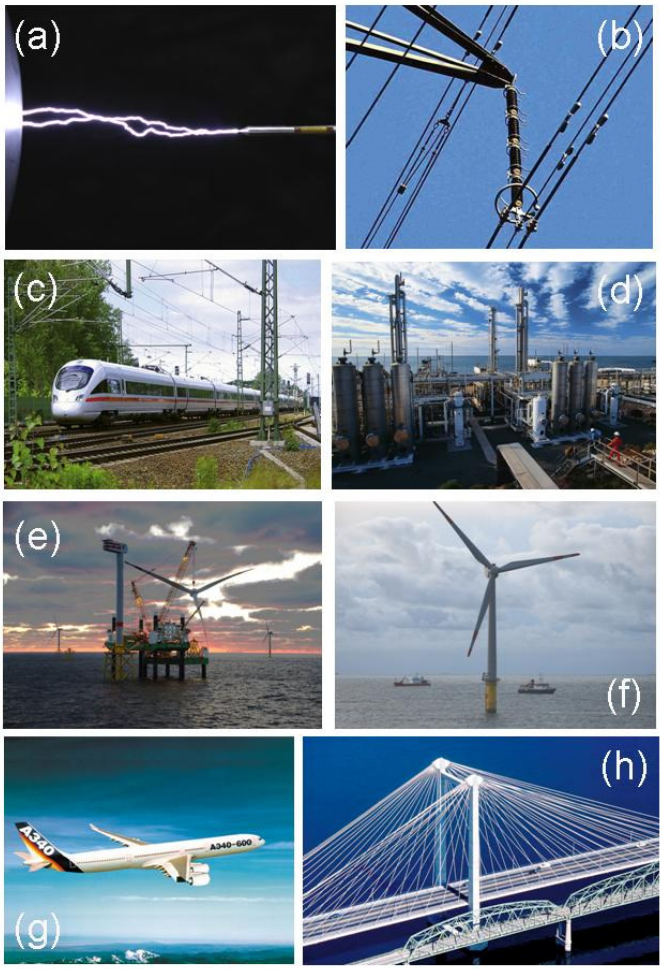

Fig. 19. Possible applications for optical strain gage technology as discussed in the text.

A major advantage of optical against electrical strain gages is the immunity with respect to electrical influences, such as illustrated in **Figs. 19a-c**, i.e. during discharges (**Fig. 19a**; optical strain gage K-OL installed on an electrode) or in high voltage wiring (**Fig. 19b**) as well as in electrical grounding as present in rails (**Fig. 19c,** see also e.g. [15]). **Fig. 19d** shows a typical environment in chemical industry where explosion detection might be required. Here, optical strain gages are preferable because they need no electric current at the inspection areas. Humidity is an important aspect in off-shore applications such as in **Fig. 19e**. Water penetration usually leads to failure (short circuits) in electrical sensors but not in optical gages. Also, optical gages are less accessible to corrosion by sea water. High strain levels often occur in wind energy rotor blades (**Fig. 19f**) and in aerospace applications (**Fig. 19g**) where fiber reinforced plastics are in use. In this case the high tensile strength of the Bragg fiber is beneficial. For survey of longer distances such as on bridges (**Fig. 19h**), the optical measurement chain avoids strong cabling efforts and cable costs because a single fiber can contain multiple sensors.

References

[1] Ch.K. Kao, Optical fiber technology, IEEE Press, New York, USA (1981);
The Nobel Prize in Physics 2009 – Press Release, Nobel Foundation, http://nobelprize.org/nobel_prizes/physics/laureates/2009/press.html;

[2] P.S. Theocaris, Moiré fringes in strain analysis, Pergamon (1969).

[3] R.P. Khetan and F.P. Chiang, Strain analysis by one-beam laser speckle interferometry, Appl. Opt. 15, 2205-2215 (1976).

[4] C. Belleville and G. Duplain, White-light interferometric multimode fiber-optic strain sensor, Opt. Lett. 18, 78-80 (1993).

[5] P.B. Tarsa, M. Brzozowski, P. Rabinowitz, and K.K. Lehmann, Cavity ringdown strain gauge, Opt. Lett. 29, 1339-1341 (2004).

[6] D. Graham-Rowe, Sensors take the strain, Nat. Photon. 1, 307-309 (2007).

[7] K.O. Hill, Y. Fujii, D. C. Johnson, and B. S. Kawasaki, Photosensitivity in optical fiber waveguides: application to reflection fiber fabrication, Appl. Phys. Lett. 32, 647-649 (1978).

[8] G. Meltz, W.W. Morey, and W.H. Glenn, Formation of Bragg gratings in optical fibers by a transverse holographic method, Opt. Lett. 14, 823-825 (1989).

[9] E. Brinkmeyer, „Faseroptische Gitter“, in: Optische Kommunikationstechnik, Eds. E. Voges and K. Petermann, Springer (2002).

[10] M.W. Rothhardt, C. Chojetzki, and H.R. Müller, High-mechanical-strength single-pulse draw tower gratings, Proc. SPIE 5579, 127 (2004).

[11] M. Kreuzer, Strain Measurement with Fiber Bragg Grating Sensors (2007), online at www.hbm.com .

[12] A. Bertholds and R. Dändliker, Determination of the individual strain optic coefficients in single mode optical fibers, J. Lightwave Tech. 6, 17-20 (1988).

[13] K. Hoffmann, An Introduction to Measurements using Strain Gages, HBM (1987).

[14] J. Zhao, X. Zhang, Y. Huang, and X. Ren, Experimental analysis of birefringence effects on fiber Bragg gratings induced by lateral compression, Opt. Commun. 229, 203-207 (2004).

[15] W. Lee, J. Lee, C. Henderson, H.F. Taylor, R. James, C.E. Lee, V. Swenson, R.A. Atkins, and W.G. Gemeiner, Railroad bridge instrumentation with fiber-optic sensors, Appl. Opt. 38, 1110-1114 (1999).

Appendix: Physical Background Information

A1. Light Guidance in Optical Fibers

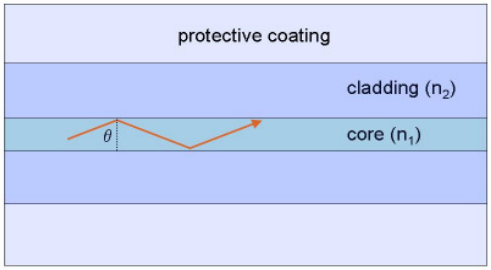

Fig. A1. Illustration of light guidance in an optical fiber. The angle θ needs to be larger than the total reflection angle θ_t.

The basic principle of optical fibers as light waveguides relies on total reflection in the fiber core with an elevated refractive index n_1 compared to the ambient medium with index n_2. In the simplest case, the fiber core is surrounded by air (n_2~1), but usually fibers cores are embedded into a cladding and further into a protective coating for mechanical and chemical protection. Normally, core and cladding have similar refractive indices n_1~n_2~1.5 for media based on silica glasses. Therefore, the total reflection angle

(A1) $$\theta_t = \arcsin\left(n_2 / n_1\right)$$

which is the lower angle limit for light wave guidance within the fiber core takes values near 90°. This in turn limits light guidance during strong fiber bending.

A2. Bragg Reflection

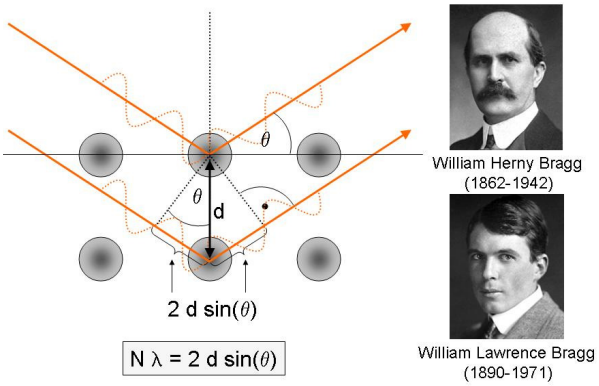

Fig. A2. Bragg reflection of light waves from a periodic crystal lattice with lattice spacing d. The optical path difference for constructive interference, $2\,d\,\sin(\theta)$, needs to fulfil the Bragg equation (framed; λ=wavelength, N=integer).

The principle of Fiber Bragg Sensors originates from Bragg reflection found by William Lawrence Bragg and his father William Henry Bragg in 1912 (both awarded with the Nobel Prize in Physics 1915): Short X-ray wavelengths in the order of atomic distances in a crystal lattice are scattered in the Bragg angle θ when the constructive interference condition for waves is fulfilled (Bragg equation):

(A2) $$N\,\lambda = 2\,d\,\sin(\theta)$$

Here, N is an integer. In other words, a multiple of the wavelengths $N\,\lambda$ needs to equal the optical path difference $2\,d\,\sin(\theta)$ between both waves in order to add to a reflection signal. This principle is also inherent to periodic Bragg gratings inscribed into an optical fiber,

however for much longer wavelengths (typically in the near-infrared regime) and only for one linear dimension. In this case, the light wave propagates normal to the Fiber Bragg Grating (θ=90°, sin(θ)=1), and the "optically effective" grating distance d is influenced by both the effective refractive index n_{eff} of the fiber core and of the inscribed grating period Λ, $d \equiv n_{eff}\ \Lambda$, as detailed in chapter 2.

A3. Optical Interference in Fiber Bragg Gratings

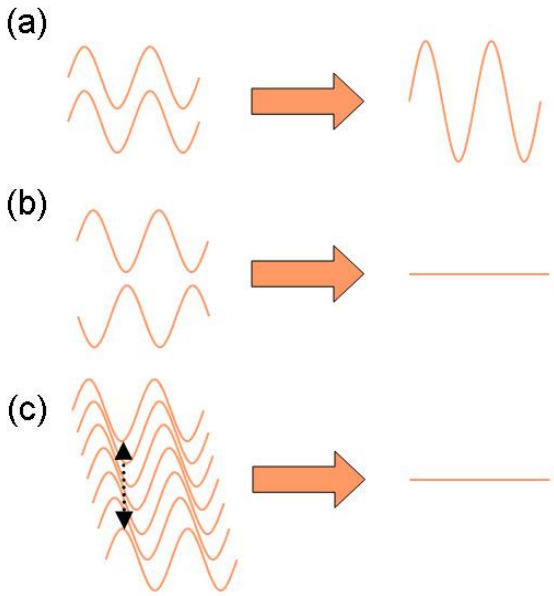

Fig. A3. Illustration of (a) constructive and (b) destructive interference of two waves, and (c) destructive interference of multiple waves with arbitrary phases.

A necessary condition to obtain the reflection signal from a Fiber Bragg Grating is constructive interference of multiple lightwaves from the grating spots.
The principle of optical interference is illustrated in **Fig. A3**. Two lightwaves with identical phase and wavelength interfere constructively to a lightwave with twice the amplitude (a). Vice versa, two lightwaves with opposites phase interfere destructively; the total signal vanishes (b). In an assemblage of wave trains with arbitrarily distributed phases (c), there are always pairs of lightwaves which interfere destructively, thus leading to a destructive signal in total.

In case of the Fiber Bragg Grating, each grating spot acts as a semi-transparent mirror reflecting a partial wave back into the fiber. Constructive interference is fulfilled when half of the Bragg wavelength λ_B fits with the grating period Λ (**Fig. A4**). Here, λ_B' is the wavelength in medium which differs from the reference wavelength in vacuum λ_B by $\lambda_B' = \lambda_B / n_{eff}$. In this case, multiple reflected waves add to a comprehensive interference signal leading to the Bragg peak. For wavelengths substantially deviating from the Bragg wavelength, the reflected waves interfere destructively and the reflection signal vanishes, alike **Fig. A3(c).**

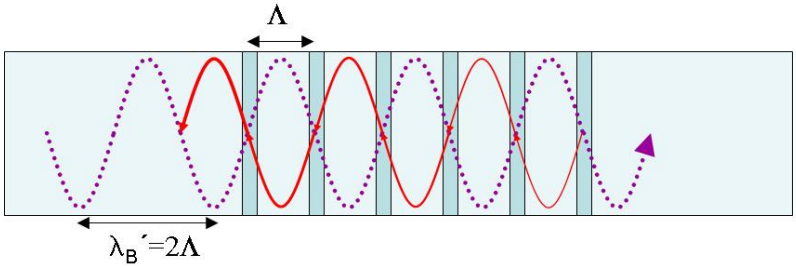

Fig. A4. Constructive interference of multiple lightwaves at the Bragg wavelength in a Fiber Bragg Grating with the grating period Λ. Dotted line: incoming wave, full line: reflects waves.